


From waves to convection and back again: The phase space of stably stratified turbulence

N. E. Sujovolsky and P. D. Mininni 

Universidad de Buenos Aires, Facultad de Ciencias Exactas y Naturales, Departamento de Física, & IFIBA, CONICET, Ciudad Universitaria, Buenos Aires 1428, Argentina



(Received 6 December 2019; accepted 13 May 2020; published 8 June 2020)

We show that the phase space of stratified turbulence mainly consists of two slow invariant manifolds with rich physics, embedded on a larger basin with fast evolution. A local invariant manifold in the vicinity of the fluid at equilibrium corresponds to waves, while a global invariant manifold corresponds to the onset of local convection. Using a reduced model derived from the Boussinesq equations, we propose that waves accumulate energy nonlinearly up to a point such that fluid elements escape from the local manifold and evolve fast to the global manifold, where kinetic energy can be more efficiently dissipated. After this, fluid elements return to the first manifold. As the stratification increases, the volume of the first manifold increases, and the second manifold becomes harder to access. This explains recent observations of enhanced intermittency and marginal instability in these flows. The reduced model also allows us to study structure formation, alignment of field gradients in the flow, and to identify balance relations that hold for each fluid element.

DOI: [10.1103/PhysRevFluids.5.064802](https://doi.org/10.1103/PhysRevFluids.5.064802)

I. INTRODUCTION

Many physical systems alternate between two states or display bistability. These systems can behave as if they were caught between a rock and a hard place, going there and back again, and in some situations the transition between states can be associated with a transition between ordered and disordered solutions. However, while finding such behavior in low-dimensional systems is not uncommon, and evidence in complex flows of similar behavior sometimes emerges, showing systematically the existence of such solutions in systems with a huge number of degrees of freedom is often impracticable. In turbulent flows, fluid elements explore a complicated phase space and may or may not go back to a previous state. Where do fluid elements go in the phase space of stably stratified turbulence, and how are they changed as they explore this space? This question has become relevant as recent observations indicate that fluid elements in stably stratified turbulence alternate between stable and unstable states, resulting in the occurrence of extreme events, enhanced intermittency, marginal instability, and critical behavior [1–6]. Moreover, a transition between different states could provide a path for efficient energy dissipation, which wave turbulence solutions often lack. However, properly answering this question requires studying the flow from a Lagrangian point of view, while most studies of this problem consider a Eulerian description of the flow.

The correct characterization of stratified turbulence is of fundamental importance for many environmental processes, as well as for weather forecasting [7,8]. In the Eulerian description, a useful way to characterize turbulent flows is through its energy spectrum and scaling relations. The presence of gravity provides a preferred direction in the system, which results in different scaling laws for the spectrum in the directions parallel and perpendicular to gravity [9–13]. The anisotropy associated with the stratification also affects velocity and temperature gradients, resulting in the generation of pancakelike structures in the flow. These structures can also be interpreted, from a spectral point of view, as resulting from a preferential transfer of energy by nonlinear

interactions toward horizontal slow modes [14–17]. The study of stratified turbulence from the Eulerian point of view has thus led to significant advances which are useful, e.g., to understand scale-by-scale balances satisfied by the system, which in turn are relevant for subgrid scale models as the production of turbulent fluctuations are ultimately controlled by velocity and buoyancy gradients.

However, important turbulent averages used to estimate mixing, such as the local shear production, the vertical buoyancy turbulent flux, and the flux Richardson number, are not obtained from the energy spectrum but from global balance equations [12,18]. A correct estimation of mixing is crucial for weather prediction, as models rely on it to estimate the effect of turbulence. But averaged values are only relevant if the statistics of the fields are Gaussian, as averages can fail to correctly capture the mixing if extreme events and localized structures are present [2–4].

In this context, a very useful approach to study mixing and dissipation in stratified turbulence is the Lagrangian description of the flow. In homogeneous and isotropic turbulence, whether it is from a single-particle approach [19] or from a multiparticle one [20], the Lagrangian perspective has been key for the understanding of several flow properties [21,22]. Both approaches have been used to study stratified turbulence in Refs. [23–27]. Vertical dispersion of Lagrangian tracers was found to be strongly suppressed when compared to the homogeneous and isotropic case [23,26], while horizontal dispersion was found to be enhanced by horizontal winds [25]. Experiments following Lagrangian buoys in the ocean have also enabled studies of dispersion and dissipation in stratified flows [28,29]. More recently, studies focused on the Lagrangian evolution of vertical gradients in stratified turbulence found a nonmonotonic enhancement of extreme events with the level of stratification [4,5,30].

Studies that combine the Lagrangian and Eulerian points of view have also proven to be useful in the study of stratified turbulence. As an example, the diffusion of a passive scalar in stratified turbulence has been modelled with an Eulerian spectral approximation by using the two-time rapid distortion theory (RDT) for predicting Eulerian correlations, and a simplified Corrsin analysis for roughly equating Eulerian and Lagrangian two-time two-point velocity correlations [31]. This study has been extended to the rapidly rotating case in Ref. [32] by means of RTD, kinematic simulations, and direct numerical simulations with inertial particles. Also, RDT has been used to study the role of two-point single-time velocity correlations in the evolution of rotating and of stratified flows in Ref. [33]. More details on these approaches can be found in Ref. [34].

Compared with homogeneous and isotropic turbulence, the Eulerian and Lagrangian descriptions of stably stratified flows are obfuscated by the presence of waves: In these flows, buoyancy acts as a restitutive force allowing for the excitation of internal gravity waves [35]. These waves play a crucial role in the development of the Eulerian spectra [9,10,14] and in the suppression of vertical transport [23,26] discussed above. As a result, many works point out the need of separating the dynamics of “waves” and of “convection” to correctly model these anisotropic flows [36]. The so-called wave-vortex decomposition achieves this by splitting the velocity field into propagating (corresponding to waves) and nonpropagating modes (associated to vortical motions), in some cases under a weakly nonlinear interaction approximation. Relevant for this work, Ref. [37] shows that the potential vorticity is better than the vertical velocity at distinguishing vortical modes from internal waves in stratified flows. Such decompositions between waves and convective motions have also been extensively used in more recent studies (see, e.g., Ref. [38]), and are reviewed in detail in Ref. [34] where the connection to poloidal-toroidal and Craya-Herring decompositions of the velocity field are also discussed.

In turbulent stratified flows, waves can also interact nonlinearly and contribute to the turbulent transfer of energy to smaller scales [39], but they can be inefficient at dissipating energy. As a result, under some conditions energy can be expected to accumulate until wavelike solutions cannot hold anymore, and the system must search in phase space for other solutions that can dissipate energy more efficiently [40,41]. The convective motions described above are a good candidate to account for such a process.

This is the main motivation for the present study. What surfaces of solutions in phase space are explored when internal gravity waves break, and how does the system fill in the gap between the different possible states? Using a reduced model for stratified flows introduced in Ref. [30], and direct numerical simulations of stably stratified turbulence, we show that the Boussinesq equations have two slow invariant manifolds corresponding to two solutions: waves, and the onset of local convection. Fluid elements stay for long times in the first region of phase space. When they escape from this manifold, they travel fast in phase space from one manifold to the other, where they can dissipate energy more efficiently, to finally return to the first manifold. Our reduced model is an extension of restricted Euler models studied in detail in homogeneous and isotropic turbulence [42–45]. These models describe the Lagrangian evolution of field gradients using a small number of ordinary differential equations, and for homogeneous and isotropic turbulence were able to explain many flow properties such as the development of intermittency and the origin of flow structures [44,45]. In spite of some limitations associated with the approximations needed to derive them [46], several advances have been made in homogeneous and isotropic turbulence to circumvent these limitations [47,48]. Moreover, as we will show, approximations needed to derive restricted Euler models in stratified turbulence are better satisfied. In our case, the reduced model allows us to also identify and study: (1) balance relations that hold for fluid elements as they are advected by the flow, (2) alignments between the vorticity, the gradient of density fluctuations, and the strain-rate tensor, and (3) correlations between different terms in the potential vorticity.

The structure of the paper is as follows. In Sec. II we introduce the Boussinesq equations, and we describe the direct numerical simulations used to study the evolution of fluid elements in phase space and to compare their evolution with the predictions from the reduced model. In Sec. III we derive in detail the restricted Euler model for stratified turbulence originally presented in Ref. [30]. In Sec. IV we study its fixed points and invariant manifolds, we compare with the results from the numerical simulations of the full Boussinesq equations, and show the evolution of fluid elements in the phase space defined by the model. Section V discusses implications of the model for subgrid modeling of stably stratified turbulence and, in particular, for the turbulent production of buoyancy gradients. Implications of the results for the alignment of field gradients are presented in Sec. VI. Section VII discusses further implications of the model for the evolution of the potential vorticity. Finally, Sec. VIII presents our conclusions.

II. THE BOUSSINESQ EQUATIONS AND DIRECT NUMERICAL SIMULATIONS

A. The equations for a stably stratified flow

In this work we will consider the Lagrangian evolution of velocity and density gradients of individual fluid elements, as they evolve under the Eulerian dynamics of an incompressible stably stratified turbulent flow. To describe the flow Eulerian dynamics we work under the Boussinesq approximation, which describes perturbations to a linear background density profile (which in our case is stable). On top of this background profile, density (or “buoyancy”) fluctuations are represented by θ . The scalar field θ has units of velocity by defining it as $\theta = g\rho/(N\rho_0)$, where g is the gravitational acceleration, ρ is the actual density fluctuation, N is the Brunt-Väisälä frequency (associated to the frequency of internal gravity waves, to the linear background density profile, and a measure of how strong stratification is), and ρ_0 is the mean background density (i.e., averaged over all space). For this scalar field and for a velocity field \mathbf{u} , the incompressible Boussinesq equations can then be written as

$$\frac{\partial \mathbf{u}}{\partial t} + \mathbf{u} \cdot \nabla \mathbf{u} = -\nabla p - N\theta \hat{\mathbf{z}} + \nu \nabla^2 \mathbf{u} + \mathbf{f}, \quad (1)$$

$$\frac{\partial \theta}{\partial t} + \mathbf{u} \cdot \nabla \theta = N\mathbf{u} \cdot \hat{\mathbf{z}} + \kappa \nabla^2 \theta, \quad (2)$$

$$\nabla \cdot \mathbf{u} = 0, \quad (3)$$

where p is the correction to the hydrostatic pressure, ν the kinematic viscosity, κ the diffusivity, and \mathbf{f} an external mechanical forcing. Equations (1) and (2) have three dimensionless parameters that control the dynamics of the system, the Reynolds, Froude, and Prandtl numbers respectively defined as

$$\text{Re} = \frac{UL}{\nu}, \quad \text{Fr} = \frac{U}{NL}, \quad \text{Pr} = \frac{\nu}{\kappa}, \quad (4)$$

where U and L are the characteristic velocity and length of the flow. While Re measures the strength of the nonlinear term compared with that of the viscous term in the momentum equation, Fr compares the strength of the nonlinear term with the buoyancy term; Pr just corresponds to the ratio of diffusivities. The strength of the turbulence is also often characterized using the buoyancy Reynolds number, defined as

$$\text{Rb} = \text{Re Fr}^2. \quad (5)$$

The Boussinesq equations have a well-known fixed point for $\mathbf{u} = \theta = 0$. Linearizing Eqs. (1) and (2) in the vicinity of this solution and neglecting viscosity and diffusivity ($\nu = \kappa = 0$), internal gravity waves are found with dispersion relation [35],

$$\omega = N \frac{k_{\perp}}{k}, \quad (6)$$

where ω is the wave frequency, $k = |\mathbf{k}|$ is the wave number, \mathbf{k} the wave vector, and k_{\perp} is the wave number associated to the components of \mathbf{k} perpendicular to gravity. In the linear regime, these waves only affect the poloidal part of the velocity field, whereas its toroidal part is disconnected from the wave regime (see Ref. [34] for more details). Note that $\omega \leq N$, and the Brunt-Väisälä frequency is thus the maximum possible frequency of internal gravity waves.

These waves play a crucial role in the dynamics of stably stratified flows, and it is known that fluid elements are often found in wavelike states in the vicinity of $\mathbf{u} = \theta = 0$. This results in low vertical diffusion and mixing [23,24,26]. However, local instabilities also play a key role in these flows. Important parameters to measure the vertical stability of the flow are given by the Richardson numbers, which have different definitions in the literature depending on whether they are estimated in the bulk or based on pointwise values of field gradients, but which in all cases attempt at estimating the ratio of production of turbulence by buoyancy to the production of turbulence by shear. Here we will consider the gradient Richardson number,

$$\text{Ri}_g = \frac{N(N - \partial_z \theta)}{|\partial_z \mathbf{u}_{\perp}|^2}, \quad (7)$$

where \mathbf{u}_{\perp} is the horizontal flow velocity (see, e.g., Ref. [49]). The factor $N - \partial_z \theta$ results from estimating the vertical derivative of the total density (or buoyancy) field $\Theta = \Theta_0 - Nz + \theta$, with Θ_0 a constant. This dimensionless number provides us with a pointwise estimation of the flow stability. When $\text{Ri}_g \leq 1/4$ the flow can undergo zigzag and shear instabilities [50], while for $\text{Ri}_g \leq 0$ the local density fluctuation can overcome the background density gradient (controlled by N) and local convection can develop, significantly increasing the vertical mixing in the vicinity of that point [26,51]. Another way to look at this latter case is the following: When $\partial_z \theta \geq N$ the local buoyancy steepness is larger in absolute value than that of the background, breaking down the vertical stability and allowing for a convective instability to take place. Finally, note that while θ should be small compared with $\Theta_0 - Nz$ for the Boussinesq approximation to be valid, there is no condition on its local vertical derivative $\partial_z \theta$ and, as a result, points with $\text{Ri}_g \leq 0$ are compatible with the approximations used in this work.

B. Numerical solutions of the Boussinesq equations and Lagrangian particles integration

We performed direct numerical simulations of Eqs. (1)–(3) in the regime of developed turbulence, in a three-dimensional (3D) periodic domain with aspect ratio $L_x:L_y:L_z = 4:4:1$ (where L_x , L_y , and

TABLE I. Characteristic parameters of the numerical simulations: N is the Brunt-Väisälä frequency, Fr is the Froude number (typical geophysical values are $Fr \approx 10^{-2}$), Re is the Reynolds number, Rb is the buoyancy Reynolds number, and L_B/η and L_{oz}/η are respectively the buoyancy scale L_b and the Ozmidov scale L_{oz} normalized by the Kolmogorov dissipation scale η .

N	Fr	Re	Rb	L_B/η	L_{oz}/η
4	0.05	10 000	25	9.6	14.4
8	0.03	14 000	13	6.0	5.6
12	0.02	15 000	4	4.0	2.8

L_z are the lengths of the domain in each direction, and with $L_x = 2\pi$ in dimensionless units), and with spatial resolution of $768 \times 768 \times 192$ grid points. We used a parallel pseudospectral fully dealiased method to compute spatial derivatives and nonlinear terms in the equations, and a second order Runge-Kutta scheme for time integration [52]. A Taylor-Green forcing was used to sustain the turbulence, a forcing that has been used in previous studies of stably stratified flows (see, e.g., Refs. [53,54]), and which is given by

$$\mathbf{f} = F_0 \left[\sin(x) \cos(y) \cos\left(\frac{L_x}{L_z} z\right) \hat{x} - \cos(x) \sin(y) \cos\left(\frac{L_x}{L_z} z\right) \hat{y} \right], \quad (8)$$

where $L_x/L_z = 4$ and F_0 is the forcing amplitude (which was chosen to have a r.m.s. flow velocity $U \approx 1$ in the turbulent steady state). The forcing generates counterrotating large scale vortices separated by planes of strong horizontal shear. In the analysis that follows, we also verified that other domain aspect ratios, other spatial resolutions, and other possible forcing schemes (see, e.g., simulations in Ref. [30]) give qualitatively similar results.

The viscosity and diffusivity ($\nu = \kappa$, and thus $Pr = 1$) were chosen so that all the relevant flow scales were properly resolved [9]. This includes the buoyancy scale $L_B = 2\pi/k_B$ (the scale associated to the typical height of the strata), the Ozmidov scale $L_{oz} = 2\pi/k_{oz}$ (the scale at which the flow starts recovering isotropy), and the Kolmogorov dissipation scale $\eta = 2\pi/k_\eta$, where all the corresponding wave numbers are respectively defined as

$$k_B = \frac{N}{U}, \quad k_{oz} = \left(\frac{N^3}{\epsilon}\right)^{1/2}, \quad k_\eta = \left(\frac{\epsilon}{\nu^3}\right)^{1/4}, \quad (9)$$

and where ϵ is the energy injection rate. The Kolmogorov dissipation scale was always slightly larger than the minimum resolved spatial scale. Three values of the Brunt-Väisälä frequency (and thus of the stratification) were considered, with $N = 4, 8,$ and 12 in dimensionless units. Resulting values of $Fr, Re, Rb,$ and of the ratios L_B/η and L_{oz}/η for the three simulations, are given in Table I.

To study the evolution of velocity and density gradients as fluid elements are advected by the fluid, in each simulation we tracked $\mathcal{O}(10^6)$ Lagrangian particles for over 10 large-scale turnover times. Each tracer satisfies the ordinary differential equation

$$\frac{d\mathbf{x}}{dt} = \mathbf{u}(\mathbf{x}, t), \quad (10)$$

where \mathbf{x} is the particle position. This equation was integrated using a Runge-Kutta method to evolve in time, and a 3D cubic spline interpolation to estimate the fluid velocity $\mathbf{u}(\mathbf{x}, t)$ at the position of the particles [55]. The same method was used to estimate velocity and temperature gradients at particles' positions, respectively denoted as $\nabla\mathbf{u}(\mathbf{x}, t)$ and $\nabla\theta(\mathbf{x}, t)$. These quantities were stored for each particle with very high time cadence. Then, finite differences and averages over multiple nearby particles (to decrease fluctuations) were used to obtain time derivatives of $\nabla\mathbf{u}(\mathbf{x}, t)$ and $\nabla\theta(\mathbf{x}, t)$, to study their evolution in phase space.

III. A REDUCED MODEL FOR THE LAGRANGIAN EVOLUTION OF FIELD GRADIENTS

From Eqs. (1)–(3) a closed model for the Lagrangian evolution of velocity and buoyancy gradients was presented in Ref. [30]. In this section we introduce a detailed derivation of this model, including intermediate equations that, albeit not closed, are in many cases exact, and useful to interpret the physical implications of the reduced model. While actual stably stratified fluids have external forcing and dissipation, for practical reasons in this section we neglect both and we consider the ideal unforced case ($\nu = \kappa = \mathbf{f} = 0$). As a result, we can expect the reduced model to give a good approximation to field gradients dynamics for short times, when the effects of the forcing and of the dissipation are small compared with other linear and nonlinear terms in the Boussinesq equations. In spite of this, we will see that the model gives useful insights into the dynamics of the full system even when long times are considered.

We start by computing spatial derivatives of Eqs. (1) and (2). We write field gradients using index notation, and define $A_{ij} = \partial_j u_i$ and $\theta_j = \partial_j \theta$ (for $i, j = \{x, y, z\}$). With this notation, we obtain

$$\frac{DA_{ij}}{Dt} + A_{kj}A_{ik} = -\frac{\partial^2 p}{\partial x_i \partial x_j} - N\theta_j \delta_{iz}, \quad (11)$$

$$\frac{D\theta_j}{Dt} + A_{kj}\theta_k = NA_{zj}, \quad (12)$$

where δ_{ij} is the Kronecker delta and $D/Dt = (\partial/\partial t + \mathbf{u} \cdot \nabla)$ is the material derivative. Equation (11) is the usual Lagrangian evolution equation for the velocity gradient tensor A_{ij} , with the extra term $-N\theta_j \delta_{iz}$ that accounts for the (linear) creation or destruction of gradients of the vertical velocity by the buoyancy gradients θ_j . Equation (12) is the Lagrangian evolution equation for buoyancy gradients. Here the nonlinear term $A_{kj}\theta_k$ represents the turbulent production or destruction of buoyancy gradients by strain and vorticity [56], while the linear term NA_{zj} corresponds to the (linear) creation or destruction of these gradients by gradients of the vertical velocity.

We can remove some of the derivatives of the pressure in Eq. (11) by using the incompressibility condition $\nabla \cdot \mathbf{u} = A_{ii} = 0$, which for the trace of Eq. (11) implies

$$A_{kl}A_{lk} = -\frac{\partial^2 p}{\partial x_l \partial x_l} - N\theta_z. \quad (13)$$

The remaining spatial derivatives of the pressure can be written using the deviatoric part of the pressure Hessian, defined as

$$H_{ij} = -\left(\frac{\partial^2 p}{\partial x_i \partial x_j} - \frac{\delta_{ij}}{3} \frac{\partial^2 p}{\partial x_k \partial x_k}\right). \quad (14)$$

Using Eqs. (13) and (14), Eq. (11) can be finally written as

$$\frac{DA_{ij}}{Dt} + A_{kj}A_{ik} - \frac{\delta_{ij}}{3}A_{kl}A_{lk} = H_{ij} - N\theta_j \delta_{iz} + N\theta_z \frac{\delta_{ij}}{3}. \quad (15)$$

This equation, together with Eq. (12), provides a set of equations (albeit not closed) for the evolution of all components of $\nabla \mathbf{u}$ and $\nabla \theta$ along the trajectories of the fluid elements.

To close this set of equations we use an approximation commonly made in restricted Euler models of homogeneous and isotropic turbulence [43–45], and we assume that the deviatoric part of the pressure Hessian can be neglected. In other words, we assume that $H_{ij} \approx 0$ in Eq. (15). In homogeneous and isotropic turbulence, recent works have focused on how to estimate this term, or on how to close it, using Gaussian random fields [46], recent deformation of Gaussian velocity fields [47], or multifractal models [48]. However, while for the homogeneous and isotropic case the condition $H_{ij} \approx 0$ is not well satisfied, in the stratified case the pressure Hessian becomes relatively smaller as stratification is increased. Moreover, attempts to close the deviatoric part of the pressure Hessian using, e.g., multifractal models, should probably be modified to take into account the anisotropy of stratified flows, and the different intermittency properties observed in their fields.

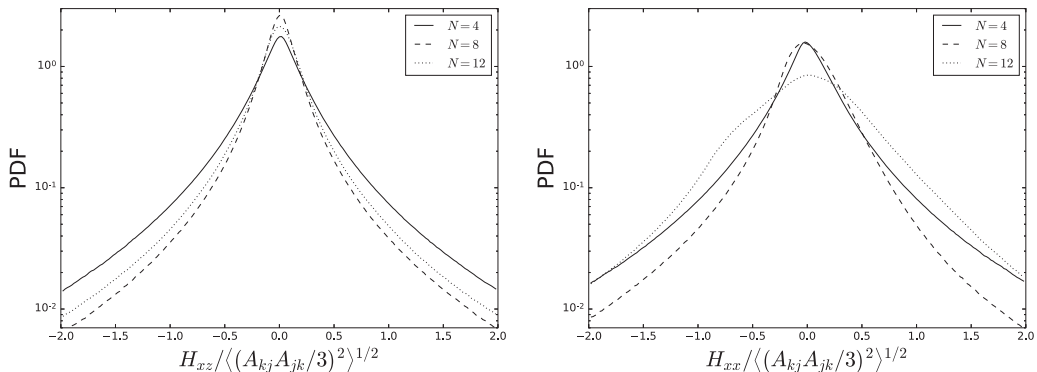


FIG. 1. PDFs of the pressure Hessian components H_{xz} (left) and H_{xx} (right), in both cases normalized by a r.m.s. typical value of one-third of the trace of the nonlinear term in Eq. (15), $\langle (A_{kj}A_{jk}/3)^2 \rangle^{1/2}$, and for the three simulations with different Brunt-Väisälä frequencies N . Note most fluid elements have relatively small pressure Hessian components, although the PDFs also display fat tails.

Thus, we will not use any of these techniques, and leave the study of their effects for the future. To partially justify this choice, and to illustrate how the contribution from the deviatoric part of H_{ij} decreases with increasing stratification, in Fig. 1 we show probability density functions (PDFs) of pointwise values of H_{xz} and H_{xx} in the direct numerical simulations in Table I, normalized by the r.m.s. value of one-third of the trace of the nonlinear term in Eq. (15), namely $\langle (A_{kj}A_{jk}/3)^2 \rangle^{1/2}$. For all simulations, more than 80% of fluid elements have normalized components of the pressure Hessian smaller than 0.2 (with an increasing percentage of these fluid elements as N increases). Note also that for $N = 12$ an asymmetry develops in the probability density functions of H_{xx} , associated with the increasing contribution of the buoyancy terms in Eq. (15). In fact, for sufficiently large N it is better to compare the amplitude of the diagonal terms of H_{ij} against these terms instead. But in any case, proper estimation of the pressure Hessian is an open problem that goes beyond this work (see, e.g., further discussions in Ref. [45]), and in spite of its apparent smaller relevance here, just as in homogeneous and isotropic turbulence we choose to neglect it in order to obtain a closed set of equations.

We also want to reduce the information in A_{ij} and θ_j to the smallest possible number of scalar quantities that result in an autonomous system. In the isotropic and homogeneous case, two scalar quantities (proportional to the traces of \mathbf{A}^2 and of \mathbf{A}^3 , with \mathbf{A} the velocity gradient tensor, and thus invariant under the group of rotations and reflections) suffice. But here, as we have more field gradients and as the stratification introduces anisotropy, the system cannot be closed with just these two variables. However, using the fact that the system has a preferred direction and that the equations are axisymmetric around this direction, we can define

$$\begin{aligned}
 Q &= -A_{ij}A_{ji}/2, \\
 R &= -A_{ij}A_{jk}A_{ki}/3, \\
 R_\theta &= \theta_i A_{ij} A_{jz}, \\
 B &= A_{zi}A_{iz}, \\
 T &= \theta_i A_{iz}, \\
 A &= A_{zz}, \\
 S &= \theta_z.
 \end{aligned} \tag{16}$$

We now want to find Lagrangian evolution equations for these seven scalars. The equations for the evolution of Q and R are well known for homogeneous and isotropic turbulence (for a derivation

of the reduced Euler model in this case, see e.g., Ref. [43]). To derive an evolution equation for Q we evaluate Eq. (15) in A_{nj} and multiply it by A_{in} . Using the derivative product rule we obtain

$$\frac{D(A_{in}A_{nj})}{Dt} + 2A_{ik}A_{kn}A_{nj} - \frac{2}{3}A_{ij}A_{kl}A_{lk} = \frac{2}{3}A_{ij}N\theta_z - N\theta_n A_{nj}\delta_{iz} - N\theta_j A_{iz}, \quad (17)$$

where H_{ij} was neglected. Setting $i = j$ in this equation we obtain $D_t Q = -3R + NT$ (where D_t is shorthand for D/Dt). To obtain an equation for R we multiply Eq. (17) by the velocity gradient tensor again, to obtain

$$\frac{D(A_{in}A_{nk}A_{kj})}{Dt} + 3A_{im}A_{mn}A_{nk}A_{kj} - (A_{in}A_{nj})(A_{kl}A_{lk}) = N\theta_z A_{ik}A_{kj} - N\theta_n A_{nj}\delta_{iz} - N\theta_j A_{iz}. \quad (18)$$

The trace of this equation results in an equation for the evolution of R , but in order to do so we need to reduce the fourth-order term $A_{im}A_{mn}A_{nk}A_{ki}$ into second-order terms. To this purpose we use the Cayley-Hamilton theorem [42,43,45], which states that any second-rank tensor V_{ij} satisfies the relation

$$V_{im}V_{mn}V_{nk} + P_V V_{il}V_{lk} + Q_V V_{ik} + R_V \delta_{ik} = 0, \quad (19)$$

where $P_V = V_{ii}$, $Q_V = -V_{kl}V_{lk}/2$, and $R_V = -V_{im}V_{mn}V_{ni}/3$. Taking $V_{ij} = A_{ij}$, then for incompressible flows $P = 0$, $Q_V = Q$, and $R_V = R$, and Eq. (19) reduces to the relation

$$A_{im}A_{mn}A_{nj} = -QA_{ij} - R\delta_{ij}. \quad (20)$$

Then, using the Cayley-Hamilton theorem, the fourth-order term in Eq. (18) can be written as $A_{im}A_{mn}A_{nk}A_{ki} = -QA_{ik}A_{ki} - R\delta_{ik}A_{ki} = 2Q^2$. By these means the equation for the evolution of R reduces to $D_t R = 2Q^2/3 + 2NSQ/3 + NR\theta$. An evolution equation for $B = A_{zi}A_{iz}$ follows in the same manner as for Q , by taking $i = j = z$ in Eq. (17), and by reducing the third-order term $A_{zk}A_{kn}A_{nz} = -QA_{zz} - R$ using again the Cayley-Hamilton theorem. Then the equation for B results $D_t B = 2QA/3 + 2R - NAS/3 - NT$. The equation for $T = \theta_k A_{kz}$ requires using both the k component of Eq. (12) multiplied by A_{kz} , and the kz component of Eq. (15) multiplied by θ_k , to obtain

$$\frac{D(\theta_k A_{kz})}{Dt} + 2\theta_m A_{mk}A_{kz} - \frac{1}{3}\theta_z A_{kl}A_{lk} = NA_{zk}A_{kz} - \frac{2}{3}N\theta_z^2, \quad (21)$$

which reduces to $D_t T = -2R_\theta - 2SQ/3 + NB - 2NS^2/3$. To derive an equation for $R_\theta = \theta_k A_{kl}A_{lz}$ we use the k component of Eq. (12) and the kz component of Eq. (17) in the same way, to compute

$$\frac{D(\theta_k A_{kl}A_{lz})}{Dt} + 3\theta_m A_{mk}A_{kl}A_{lz} - \frac{2}{3}\theta_k A_{kz}A_{kl}A_{lk} = -\frac{4}{3}N\theta_z\theta_n A_{nz} + NA_{zk}A_{kl}A_{lz}. \quad (22)$$

To express this equation in terms of our scalar quantities, we use again the Cayley-Hamilton theorem in Eq. (20) for $A_{mk}A_{kl}A_{lz} = -QA_{mz} - R\delta_{mz}$ and $A_{zk}A_{kl}A_{lz} = -QA_{zz} - R$. Then the evolution equation for R_θ results $D_t R_\theta = 5QT/3 + 3RS - 4NST/3 - NQA - NR$. Finally, the equation for A is obtained by simply taking $j = i = z$ in Eq. (15), resulting in $D_t A = -B - 2Q/3 - 2NS/3$, and the equation for S is obtained by taking $j = z$ in Eq. (12), resulting in $D_t S = NA - T$.

The resulting reduced model for the Lagrangian evolution of field gradients of stratified turbulence can be summarized as

$$\begin{aligned}
 D_t Q &= -3R + NT, \\
 D_t R &= 2Q^2/3 + 2NSQ/3 + NR_\theta, \\
 D_t R_\theta &= 5QT/3 + 3RS - 4NST/3 - NQA - NR, \\
 D_t B &= 2QA/3 + 2R - NAS/3 - NT, \\
 D_t T &= -2R_\theta - 2SQ/3 + NB - 2NS^2/3, \\
 D_t A &= -B - 2Q/3 - 2NS/3, \\
 D_t S &= NA - T.
 \end{aligned} \tag{23}$$

This system prescribes the evolution of field gradients along the trajectories of the fluid particles. From the frame of reference of a Lagrangian particle, these equations are a closed system of seven ordinary differential equations. As in the reduced Euler model of homogeneous and isotropic turbulence, the only approximations made to derive the equations were to assume an ideal and unforced regime, and to neglect the pressure Hessian H_{ij} . In the reduced Euler case, dropping H_{ij} makes field gradients to diverge and the system to blow up in finite time. In our system stratification slows down the blow up, and can prevent it in some cases if N is large enough [30]. Nevertheless, the dynamics of this system, even when it blows up at finite time, provides significant information on the dynamics of the full set of partial differential Eqs. (1)–(3), as we will show in the following sections.

IV. EVOLUTION OF FLUID ELEMENTS IN PHASE SPACE

In this section we characterize the topological properties of the phase space of the reduced system in Eq. (23), and we compare its predictions with those obtained from the time evolution of field gradients in the direct numerical simulations of the full Boussinesq equations. From the simulations in Table I we compute Q , R , R_θ , T , B , A , and S for all fluid elements, and their time derivatives, and embed these quantities in the phase space defined by the reduced model. Compared with previous results presented in Ref. [30], here we will not only study whether fluid elements in the full system accumulate in certain regions of the phase space of the reduced system but also how fast or slow they evolve depending on the region in which they are.

This section is organized as follows: First, we introduce the fixed points of the system, for which the time derivatives of all the scalars are zero. Associated to fixed points, dynamical systems can have invariant manifolds, which are constrained regions of the phase space where points (i.e., states of the system) can only evolve to other points in the same manifold. In these manifolds, the dimensionality of the system is further reduced [57]. We consider the invariant manifold that is known to play a relevant role in the homogeneous and isotropic case, and study how stratification modifies this manifold and introduces new invariant manifolds. Finally, after discussing the role of these manifolds and their physical relevance, we propose a simplified picture of the phase space of stably stratified turbulence.

A. Fixed points

We start by listing the fixed points of the reduced model for the Lagrangian evolution of field gradients. The system in Eq. (23) has two sets of fixed points,

$$\begin{aligned}
 \text{I} : Q = R = R_\theta = T = B = A = S = 0, \\
 \text{II} : R_\theta = \frac{2N^2 Q - 6Q^2}{3N}, \quad B = \frac{2N^2}{3} - 2Q, \quad T = \frac{3R}{N}, \quad A = \frac{3R}{N^2}, \quad S = \frac{2Q}{N} - N, \quad Q, \text{ and } R \text{ free.}
 \end{aligned} \tag{24}$$

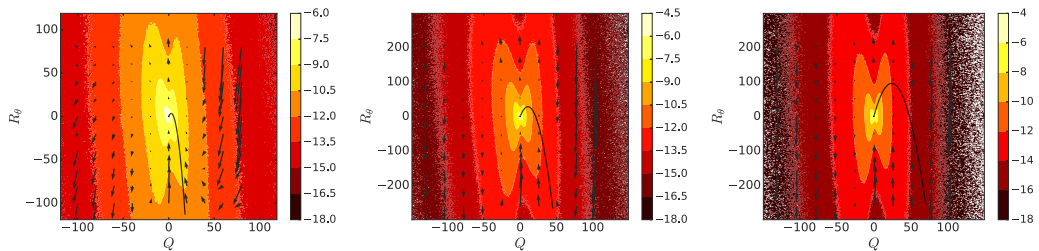


FIG. 2. Joint probability density functions of Q and R_θ for $N = 4, 8,$ and 12 (from left to right). Colors represent the probability density of finding fluid elements with the corresponding values of Q and R_θ in the numerical simulations of the Boussinesq equations (color tables here and in the following figures are in log scale), while the arrows indicate the direction and speed in which fluid elements evolve on the average. The relation $R_\theta = (2N^2Q - 6Q^2)/(3N)$, associated with fixed point I, is shown as reference with a solid line.

Fixed point I corresponds to null gradients of \mathbf{u} and θ . Unlike the fixed point $Q = R = 0$ in the reduced Euler model for homogeneous and isotropic turbulence (i.e., for $N = 0$, see Refs. [42–45] and the discussion below), this fixed point is not obviously unstable. When the system in Eq. (23) is linearised around this fixed point, the linear system of ordinary differential equations can be represented by a matrix whose eigenvalues provide information of how fluid elements evolve when perturbed in its vicinity. The array has one eigenvalue equal to 0, four eigenvalues equal to $\pm iN$, and two eigenvalues equal to $\pm i\sqrt{6}N/2$. As all eigenvalues are zero or purely imaginary, small perturbations around fixed point I results in oscillations (between linear combinations of $Q, T, B,$ and S in one case and A and S in the other). Also because all eigenvalues are zero or purely imaginary, center manifold theory can be used to further reduce the dimensionality of the system [57] (see Sec. IV C). Physically, this fixed point corresponds to the stratified fluid at equilibrium, and linearly perturbing this solution results in the excitation of internal gravity waves as follows from Eq. (6). The behavior described here is the counterpart for field gradients of the well-known fixed point of the full Boussinesq partial differential equations for $\mathbf{u} = \theta = 0$ [35]. Of course, if the fluid elements are perturbed far from this equilibrium, nonlinearities will become relevant and fluid elements may run away in phase space.

The other solution, fixed point II, actually corresponds to a manifold of fixed points, as Q and R are free (i.e., for each value of these variables we have a fixed point in the system). To confirm their presence in the full Boussinesq partial differential equations, Fig. 2 shows the joint probability density function of R_θ and Q (i.e., the probability density of finding fluid elements with different values of these two variables) obtained from the direct numerical simulations, with arrows indicating the mean direction and speed at which fluid elements evolve in this plane (also obtained from the full Boussinesq system). Superimposed, we show the relation $R_\theta = (2N^2Q - 6Q^2)/(3N)$ which corresponds to fixed points II of the reduced model. There is a correlation between points in the direct numerical simulations and this relation, in the sense that arrows are small in the vicinity of the fixed points (albeit there is no significant accumulation of fluid elements in the manifold defined by these fixed points). Other lobes showing significant accumulation of probability, as well as other regions with slow evolution (i.e., with small arrows, or equivalently, with small DR_θ/Dt and DQ/Dt) are associated to projections into this R_θ - Q plane of slow manifolds in the reduced system that will be discussed next (note these figures, and all following figures, correspond to projections into planes of a seven-dimensional phase space).

B. The Vieillefosse manifold

As mentioned before, an invariant manifold is a region of phase space that is invariant under the action of the dynamical system (i.e., such that initial conditions in this manifold remains in the same manifold as time evolves). These manifolds are often constructed by perturbing dynamical

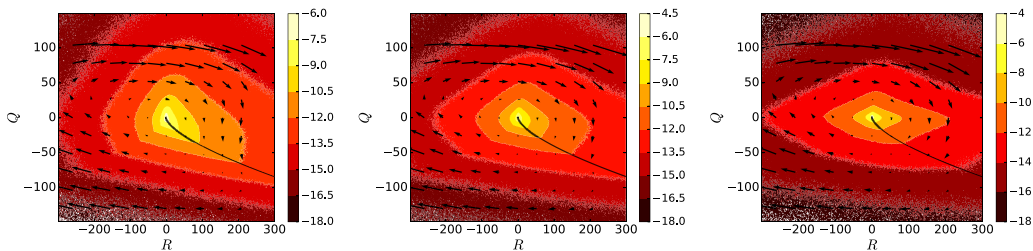


FIG. 3. Joint probability density function of Q and R for $N = 4, 8,$ and 12 (from left to right). Colors represent the logarithm of the probability density of finding fluid elements with the corresponding values of Q and R in the numerical simulations of the Boussinesq equations, while the arrows indicate the averaged direction and speed in which fluid elements evolve. The Vieillefosse tail $Q = -(27/4R^2)^{1/3}$ is shown as reference with solid lines. For homogeneous and isotropic turbulence, this curve corresponds to an invariant manifold of the Q - R reduced Euler model.

systems around fixed points, although global invariant manifolds (i.e., valid up to any order in the nonlinearity) can also exist.

In the case with $N = 0$ (no stratification, homogeneous, or isotropic flows), the reduced system in Eq. (23) further reduces to the so-called Vieillefosse or reduced Euler model for Q and R (which are the two rotationally invariant scalars obtained from the traces of \mathbf{A}^2 and \mathbf{A}^3 , and proportional to sums and products of the eigenvalues of the A_{ij} tensor) [42–45],

$$\begin{aligned} D_t Q &= -3R, \\ D_t R &= 2Q^2/3, \end{aligned} \quad (25)$$

and also to a reduced system of ordinary differential equations for the gradients of an isotropic passive scalar. The system in Eqs. (25) has only one fixed point, $Q = R = 0$, and one invariant manifold, the so-called Vieillefosse tail given by $Q = -(27/4R^2)^{1/3}$ [42,45], as it can be shown that $D_t(4Q^3/27 + R^2) = 0$. The reduced Euler system blows up following this manifold, with gradients growing to arbitrarily large (negative) values of Q . However, this manifold plays a crucial role in the dynamics even in the viscous and forced Navier-Stokes case, as it can be shown that its existence is associated with the observed alignment of vorticity with an eigenvector of the strain-rate tensor, with the phenomenon of vortex stretching, and with the development of extreme events in the flow [45,56,58,59].

In the stratified case ($N \neq 0$), from the reduced system in Eq. (23) this relation is replaced by

$$\frac{D}{Dt} \left(\frac{4Q^3}{27} + R^2 \right) = \frac{3N}{2} [3NR(3B + 2Q) + 2Q^2T], \quad (26)$$

and thus, as N increases from zero, this manifold stops being invariant and it becomes less relevant for the dynamics. Indeed, in the direct numerical simulations we observe that for small values of N some fluid elements still accumulate near this manifold but that this accumulation decreases as N increases. To illustrate this, Fig. 3 shows the isocontours of the joint probability density functions of Q and R for all simulations. Besides the change in the PDFs, there is also a change in the rate of change of Q and R : For $N = 4$ vectors are small near the Vieillefosse tail and tend to align with this manifold in its vicinity. Instead, for $N = 8$ and 12 , although fluid elements still slow down near the manifold, they cross it and they orbit around the point $Q = R = 0$. This corresponds, as mentioned above, to the wavelike motions near fixed point I and also indicates that the mechanism of vortex stretching (see, e.g., Refs. [58,59]) is significantly affected by the stratification, in agreement with the well-known change in the geometry of vortical structures in stably stratified turbulence from

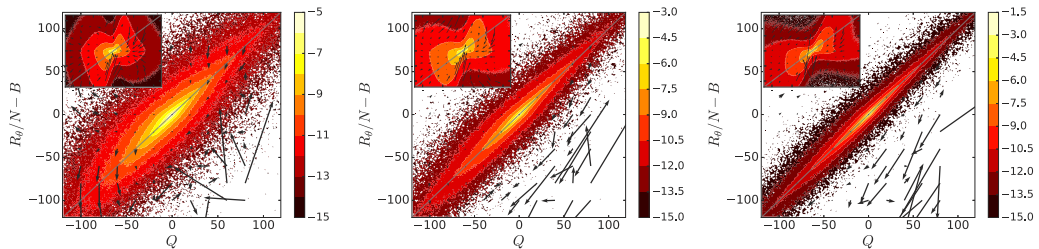


FIG. 4. Joint probability density function of $R_\theta/N - B$ and Q for simulations of the full Boussinesq equations with $N = 4, 8,$ and 12 (from left to right), restricted to fluid elements with $S \approx 0$. Arrows indicate the mean rate of change of these quantities in the direct numerical simulations. The invariant manifold Σ_I with $Q = R_\theta/N - B$ is shown as a reference by solid lines. Insets show the same quantities but for all fluid elements (i.e., without any restriction on the possible value of S), and with the same ranges for the axes as the main figures. Insets in the following figures also follow this convention.

tubes to pancakes. Indeed, note that Q can be written as [59]

$$Q = \frac{1}{4}[\boldsymbol{\omega}^2 - 2 \text{Tr}(\mathbf{s}^2)], \quad (27)$$

where $\boldsymbol{\omega} = \nabla \times \mathbf{u}$ is the vorticity, Tr denotes the trace, and $\mathbf{s} = (\mathbf{A} + \mathbf{A}^T)/2$ is the strain-rate tensor. As a result, fluid elements with $Q > 0$ are dominated by vorticity, and fluid elements with $Q < 0$ are dominated by strain. Also, for $R > 0$ flow topologies are stable, while for $R < 0$ flow topologies are unstable. Finally, it can be also shown (see, e.g., Ref. [59]) that regions in Fig. 3 with $R > 0$ and $Q > 0$ correspond to unstable compression of vortices, regions with $R > 0$ and Q below the Vieillefosse tail correspond to unstable vortex sheet structures, and regions with $R < 0$ correspond to stable tubelike structures (which can be also stretched depending on the value of Q). Thus, the apparent accumulation (for sufficiently large N) of fluid elements near $Q \approx 0$ and with any sign of R seems to indicate structures alternate between all these possible configurations in the stably stratified case (the local structure of the flow will be discussed in more detail in Sec. VI).

C. The invariant manifold in the vicinity of fixed point I

An expansion of the ordinary differential equations in Eq. (23) in the vicinity of fixed point I shows that

$$\Sigma_I : \frac{D}{Dt} \left(\frac{R_\theta}{N} - B - Q \right) = 0, \quad (28)$$

i.e., $R_\theta/N - B - Q = 0$ is a local invariant manifold of the system.

Figure 4 shows the joint probability density functions of $R_\theta/N - B$ and Q for the direct numerical simulations, together with arrows indicating the mean rate of change of these quantities in the phase space, only for fluid elements with $S \approx 0$ (as expected near fixed point I), using the same criteria for the selection of fluid elements as in Ref. [30] (briefly, here and in the following conditions $S \approx 0$ or $S \approx N$ mean all particles satisfying any of these conditions within 10% of the value of N were chosen). The insets in Fig. 4 show the same probability density functions but without any restriction on the values of S . For the restricted cases, and for all simulations with different values of N , a strong correlation between $R_\theta/N - B$ and Q is seen, as evidenced by the larger probability densities near the manifold $R_\theta/N - B = Q$. Moreover, the correlation increases with increasing N . And this correlation is seen even for large values of $R_\theta/N - B$ and Q , in spite of the fact that the invariant manifold is local (i.e., only expected to be valid in the vicinity of the fixed point I).

Rates of change are very small near the invariant manifold $R_\theta/N - B = Q$, and large far from it, more clearly in the simulation with $N = 12$ (note the disparate size of the arrows in different regions of phase space in Fig. 4). This suggests that fluid elements evolve slowly near this manifold, or in

other words, that the local manifold Σ_I is not only preserved in the full Boussinesq system but is also a slow manifold of the system.

D. The invariant manifold in the vicinity of fixed point II

Only valid in the vicinity of fixed point II, the system in Eq. (23) has two invariant manifolds,

$$\begin{aligned}\Sigma_{II,a} : Q &= \frac{N^2}{3}, \quad R \text{ free}, \quad \frac{D}{Dt}(-4R + NT + N^2A) = 0, \\ \Sigma_{II,b} : Q &= -\frac{N^2}{3}, \quad R \text{ free}, \quad \frac{D}{Dt}\left(R_\theta - NB + \frac{8NQ}{3}\right) = 0.\end{aligned}\quad (29)$$

But in order to reach fixed points II, the system needs a value of Q or B of $O(N^2)$, so this set of fixed points are hard to access. Indeed, analysis of the direct numerical simulations indicate that the invariant manifolds associated with fixed points II do not seem to have a relevant role in the dynamics of the fluid elements.

E. The global invariant manifold

From the system in Eq. (23), it can be verified that $T = NA$, $S = N$, and $R_\theta = NB$ is a global invariant manifold as

$$\Sigma_0 : D_t(T - NA) = 0, \quad D_t S = 0, \quad D_t(R_\theta - NB) = 0. \quad (30)$$

This particular manifold is valid for all orders of the nonlinearity, and inside it, the system in Eq. (23) reduces to a dynamical system with just 4 degrees of freedom,

$$\begin{aligned}D_t Q &= -3R + NT, \\ D_t R &= N^2 B + 2N^2 Q/3 + 2Q^2/3, \\ D_t B &= -4N^2 T/3 + 2NR + 2QT/3, \\ D_t T &= -NB - 2N^3/3 - 2NQ/3.\end{aligned}\quad (31)$$

This manifold has a rich physical interpretation, since as $S = \partial_z \theta$, then for $\partial_z \theta = N$ the gradient Richardson number in Eq. (7) becomes zero, and fluid elements in this manifold are at the onset of the convective instability becoming vertically unstable at the slightest perturbation. Thus, and although stably stratified turbulence is expected to display low vertical mixing [24,60] and wavelike solutions, fluid elements in Σ_0 can display a marginal instability as reported for stratified turbulence in Refs. [1,6], go through bursts and trigger sudden and intermittent local convective processes as observed in Refs. [2–5], and significantly enhance vertical dispersion as reported in Refs. [26].

Figure 5 shows the joint PDFs of R_θ and NB , while Fig. 6 shows the joint PDFs of NA and T , obtained from the direct numerical simulations, and superimposed with mean rates of change of all quantities. As references, we also indicate in these figures the relations $T = NA$ and $R_\theta = NB$ of the global invariant manifold Σ_0 . The correlation of the dynamics of fluid elements in the numerical simulations with this manifold improves when fluid elements are restricted to cases with $S \approx N$ (as expected for Σ_0). Moreover, fluid elements again evolve slowly in the vicinity of this manifold. A slow evolution, and the accumulation of fluid elements near this manifold, can be explained as the evolution of the convective instability (which takes place in the order of the turnover time) is slower than the fast internal gravity waves and other physical processes in the flow.

F. Overall dynamics

The data from the direct numerical simulations presented so far indicates that fluid elements spend a significant time exploring two invariant manifolds. Moreover, the data also shows that as

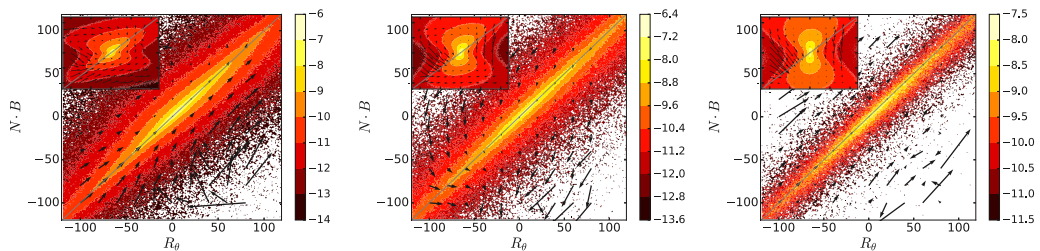


FIG. 5. Joint probability density function of NB and R_θ for direct numerical simulations with $N = 4, 8,$ and 12 (from left to right), together with arrows indicating mean rate of change of these quantities, restricted to fluid elements with $S \approx N$. The curve $NB = R_\theta$, corresponding to the invariant manifold Σ_0 , is indicated as a reference by the solid lines. Insets show the same quantities but for all fluid elements (without any restriction on the possible value of S).

N increases, the local invariant manifold Σ_1 holds a larger fraction of particles, as opposed to the global manifold which holds a smaller fraction of fluid elements. This is shown in Fig. 7, which shows the percentage of fluid elements at any moment with $S \approx 0$ or with $S \approx N$ in all simulations in Table I, as a function of Fr . However, note that previous studies [4,30] suggest that this behavior may be monotonous only for sufficiently large N (or sufficiently small Fr), while for intermediate values of N fluid elements could escape more rapidly (and nonmonotonously with N of Fr) from the local invariant manifold.

The present analysis also indicates that once fluid elements escape from any of these two manifolds, the evolution of fluid elements is fast as they move in phase space from one manifold to the other. This is not only suggested by the reduced model, but also seen in the data from the simulations of the full Boussinesq equations. Indeed, as shown above, the invariant manifolds are not only partially preserved in the full system, but are also slow, as rates of change of field gradients in phase space decrease dramatically in the vicinity of these manifolds. Moreover, fluid elements display fast and extreme values of the gradients when $S \neq 0$ or N , and in these cases the fluid elements seem to rapidly recover one of these two values. This is also illustrated in Fig. 8, where the value of S is shown as a function of time for an individual fluid element in the simulation with $N = 4$. Note S fluctuates around 0 or 4 for long times, and changes between these two values are often mediated by a long and fast excursion in the value of S (we will see similar alternations between slow and fast evolution in the dynamics of the potential vorticity in Sec. VII).

Following these results, we propose the following scenario: The phase space of stably stratified turbulence is composed of two main slow invariant manifolds. The local manifold Σ_1 , valid in

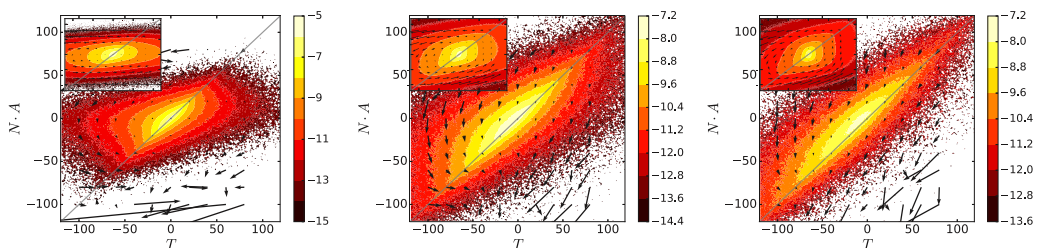


FIG. 6. Joint probability density function of NA and T for direct numerical simulations with $N = 4, 8,$ and 12 (from left to right), together with arrows indicating mean rate of change of these quantities, restricted to fluid elements with $S \approx N$. The curve $NA = T$, corresponding to the invariant manifold Σ_0 , is indicated as a reference by the solid lines. Insets show the same quantities but for all fluid elements (without any restriction on the possible value of S).

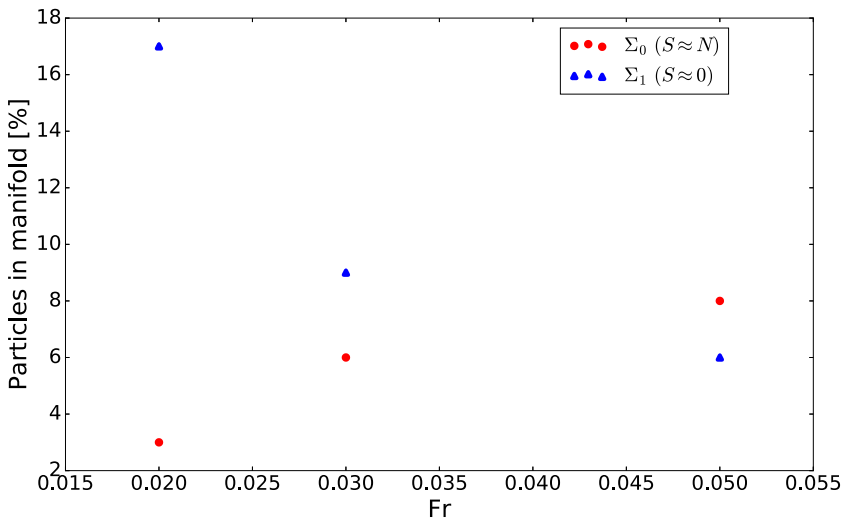


FIG. 7. Fraction of fluid elements (in percentage) in manifolds Σ_0 (with $S \approx N$) and Σ_l (with $S \approx 0$) as a function of Fr , for all simulations in Table I (i.e., for $N = 12, 8, \text{ and } 4$, in that order with increasing Fr). Notice how the percentage of fluid elements in the wavelike invariant manifold (Σ_l) decrease with increasing Fr , while the percentage of fluid elements at the onset of convection (i.e., in Σ_0) increase with increasing Fr , at least for the values of Re considered here.

the proximity of the flow at equilibrium (fixed point I) corresponds to the case in which waves dominate the system dynamics. When energy in the waves grows too much (either from nonlinear amplification, from the wave turbulence cascade, or from effects neglected in the reduced model such as forcing or pressure gradients), fluid elements can escape this local manifold and explore

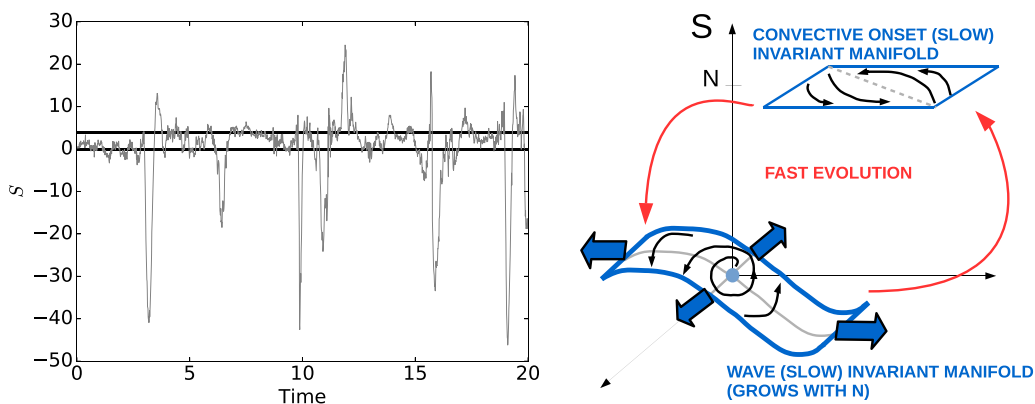


FIG. 8. Left: Value of S as a function of time for one particle in the simulation with $N = 4$. Horizontal lines with $S = 0$ and $S = N = 4$ are shown as references. The particle spends more time near these two values, with fast bursts and excursions in between. Right: Schematic of the proposed dynamics of fluid elements of the full Boussinesq system embedded in the phase space of the reduced system. For simplicity, the seven-dimensional phase space is represented with only three axes. Fluid elements spend a long time in a “wavy” state in the slow invariant manifold Σ_l with $S \approx 0$ and $Q \approx R_\theta/N - B$ (whose size grows with N). As their energy increases, fluid elements eventually escape from Σ_l and evolve fast toward the global invariant manifold Σ_0 with $S \approx N$, $T \approx NA$, and $R_\theta \approx NB$. Fluid elements in this manifold are at the brink of the convective instability, and any perturbation results in efficient dissipation and in the fast return of fluid elements to the first invariant manifold.

(fast) the phase space until finding the global slow manifold Σ_0 . When this happens, the wave turbulence solutions break, and the finding of Σ_0 can be interpreted as the result of fluid elements looking for a different surface of solutions in phase space to efficiently dissipate their energy. Manifold Σ_0 is at the brink of the local convective instability. Any perturbation from this manifold excites local convection, and the full Boussinesq equations can dissipate energy through strong turbulence mechanisms. Then, particles can rapidly go back to the first local manifold Σ_1 and be dominated again by the waves. These two manifolds, which the particles can inhabit for long periods of time, are embedded in a phase space in which particles evolve fast, and which fills the gap between the stable wavelike regime and the efficient dissipation of accumulated energy (see the diagram in Fig. 8). In this scenario, as N increases, the size and stability of Σ_1 can be also expected to increase (see Fig. 4 and Ref. [30] for a confirmation of this behavior), resulting in less and less excursions to the strongly nonlinear region of phase space associated with the Σ_0 manifold.

V. TURBULENT PRODUCTION OF VERTICAL BUOYANCY FLUCTUATIONS

We can now discuss some of the physical implications of the behavior reported in the previous section for the modeling of stably stratified turbulence, for the formation of flow structures, and for the evolution of important quantities in geophysical flows such as the potential vorticity. Let us start with turbulent production of buoyancy fluctuations, which affects dissipation and is important for mixing and for subgrid scale models. The z component of Eq. (12) can be written as

$$\frac{D\theta_z}{Dt} = -A_{kz}\theta_k + NA_{zz}, \quad (32)$$

and gives the evolution of the vertical buoyancy gradients as seen when following fluid element trajectories in the ideal Boussinesq equations. In this equation, the production and destruction of vertical buoyancy gradients are controlled by strain and rotation (associated with the vorticity) as described by the term $-A_{kz}\theta_k = -T$, and by the buoyancy term $NA_{zz} = NA$. For fluid elements in the global invariant manifold Σ_0 (i.e., for fluid elements at the brink of convection), the two terms are balanced (as $T = NA$), and Eq. (32) reduces to $D_t\theta_z = 0$. In physical terms, production of vertical buoyancy gradients by turbulence is perfectly balanced by linear (buoyancy) effects.

Moreover, in the global invariant manifold Σ_0 , as $\theta_z = S = N$ does not vary, we can derive another balance relation for buoyancy gradients, which has important consequences for subgrid modeling as it provides a condition over the turbulent dissipation of spatial buoyancy variations. Multiplying Eq. (12) by θ_j we obtain the following equation for the second-order one-point correlation of buoyancy gradients,

$$\frac{1}{2} \frac{D(\theta_j\theta_j)}{Dt} = -\theta_k\theta_j A_{kj} + N\theta_j A_{zj}. \quad (33)$$

For $i = j$ this equation gives the evolution of $|\nabla\theta|^2$ which (after integrating over the whole volume) controls the total dissipation of potential energy in the flow $E_p = \int \theta^2/2 dV$ (see, e.g., Ref. [61]). As a result, this equation often appears in subgrid models of stratified turbulence [56].

The first term on the right-hand side of Eq. (33), $-\theta_k\theta_j A_{kj}$, corresponds to the turbulence production term [56], while the second term, $N\theta_j A_{zj}$, accounts again for buoyancy effects. We can expect the time derivative on the left-hand side of Eq. (33) to become small when a fluid element is close to any of the two invariant manifolds, as time evolution becomes slow in these manifolds. For the particular case of manifold Σ_0 , in which turbulence and field gradients can be expected to be more relevant, neglecting the time derivative in Eq. (33) implies that as long as particles remain in this manifold, then

$$\theta_k\theta_j A_{kj} \sim N\theta_j A_{zj} \sim ST. \quad (34)$$

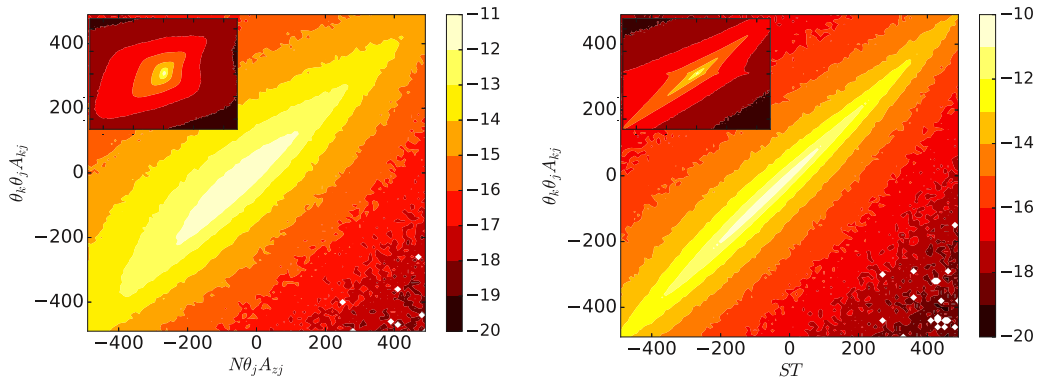


FIG. 9. Joint probability density function of $\theta_k \theta_j A_{kj}$ and $N \theta_j A_{zj}$ (left) and of $\theta_k \theta_j A_{kj}$ and ST (right) for fluid elements with $S \approx N$ in the simulations with $N = 8$. The insets show the same quantities but for fluid elements without any restriction on the values S can take.

This relation implies that also for the second-order one-point correlation of buoyancy gradients, turbulent production is approximately balanced by buoyancy effects. And if this relation holds in the numerical data, it also confirms that $|\nabla\theta|^2$ varies slowly in the Σ_0 manifold.

Figure 9 shows the joint probability density functions of $\theta_k \theta_j A_{kj}$ and $N \theta_j A_{zj}$, and of $\theta_k \theta_j A_{kj}$ and TS , for fluid elements close to the Σ_0 invariant manifold in the simulation of the full Boussinesq equations with $N = 8$ (the insets show the same probability density functions for all fluid elements in the flow, irrespectively of their value of S). The observed correlations are in good agreement with Eq. (33), and indicate a possible way to estimate relevant subgrid production terms using the reduced model.

VI. ALIGNMENT OF FIELD GRADIENTS AND LOCAL FLOW GEOMETRY

In homogeneous and isotropic turbulence, the existence of the Vieillefosse invariant manifold in the restricted Euler model (dependent only in the variables Q and R) has implications for the alignment of the vorticity with one of the principal axes of the strain-rate tensor, and as a result, with the formation of vortical structures through vortex stretching [45,58,59]. As was discussed in Sec. III, the replacement of the Vieillefosse tail by two other invariant manifolds in the system in Eq. (23) should have an important effect in vortex stretching and in the development of structures in stably stratified flows. These effects are discussed in this section, by studying the alignment of the vorticity and of buoyancy gradients with the principal axes of the strain-rate tensor, as well as with the Cartesian axes, paying special attention to directions parallel and perpendicular to gravity.

In the context of this analysis, we can study separately the two relevant regions of the phase space of stably stratified turbulence by discriminating fluid elements which have (instantaneously) $S \approx 0$ or $S \approx N$. We can also study alignment globally (i.e., for all fluid elements) by considering fluid elements in the entire flow, without any restriction on the value of S . As mentioned, we will consider the vorticity $\boldsymbol{\omega}$ at the position of each of these fluid elements, the density gradient $\nabla\theta$, and the strain-rate tensor defined as in Sec. IV B as

$$s_{ij} = \frac{1}{2}(A_{ij} + A_{ji}). \quad (35)$$

This symmetric tensor describes the rate at which fluid elements are stretched and sheared. It has three eigenvalues s_α , s_β , and s_γ (with decreasing value, and with the eigenvalue s_γ being negative). Each eigenvalue is associated to an eigenvector, respectively $\boldsymbol{\alpha}$, $\boldsymbol{\beta}$, and $\boldsymbol{\gamma}$, which are orthogonal and define the principal axes of stretching and shearing. In fact, the three eigenvalues correspond to the strain along these principal axes, so that fluid elements along these directions are locally strained

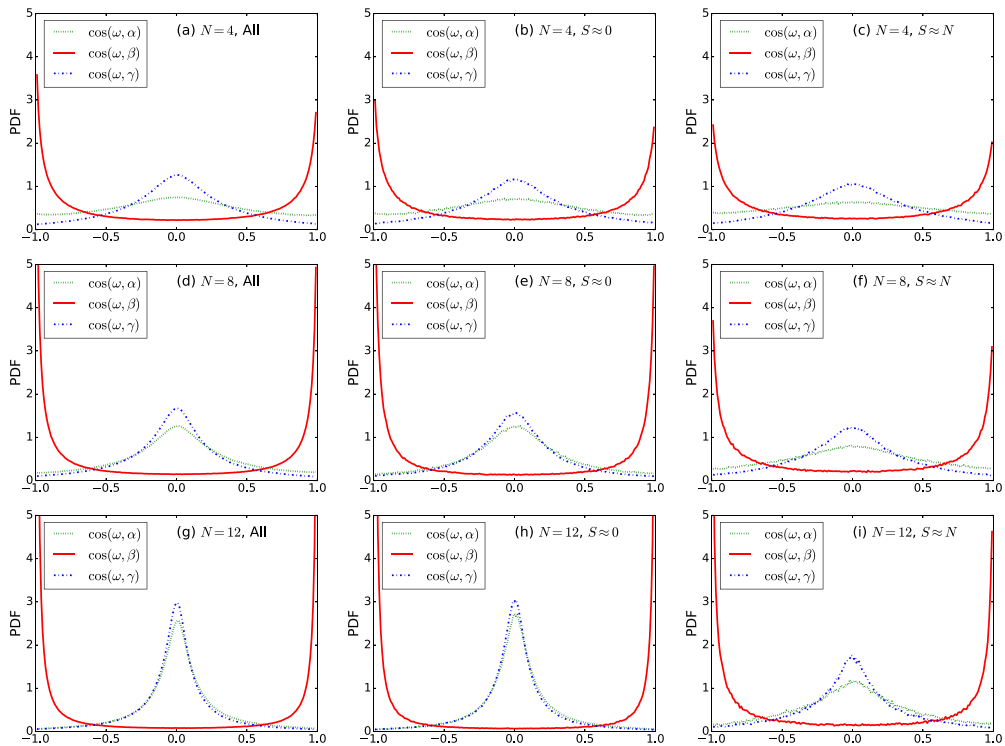


FIG. 10. PDFs of the cosine of the angles between the vorticity ω and the eigenvectors α , β , and γ of the strain rate tensor s_{ij} . In the first row, panels (a)–(c) correspond to simulations with $N = 4$, with panel (a) showing the PDFs of all fluid elements (i.e., without any restriction on the value of S), panel (b) showing fluid elements restricted to instants with $S \approx 0$, and panel (c) restricted to $S \approx N$. The second row, with panels (d)–(f), shows the same PDFs for the simulation with $N = 8$, while the third row, with panels (g)–(i), shows the case with $N = 12$.

but not rotated. Studying the alignment between these quantities then reduces to studying the angles between the vectors ω , $\nabla\theta$, α , β , and γ .

In homogeneous and isotropic turbulence vorticity ω aligns with the intermediate strain eigenvector β . In other words, vorticity is driven away from the direction of compression (associated to γ), resulting in vortex stretching at an intermediate rate (as in practice $s_\beta > 0$, but smaller than s_α). A restricted Euler model of the vorticity-shear interaction suggest that, as this process takes place in a time shorter than the eddy turnover time, the alignment of ω with β is the result of angular momentum conservation [45,56,62]. This is also the case for stably stratified turbulence (albeit with a dependence on the level of stratification), as is shown in Fig. 10. The figure shows the PDFs of the cosine of the angle between ω and the eigenvectors α , β , and γ of the strain-rate tensor, for the simulations with $N = 4, 8$, and 12 , and for all fluid elements, as well as for fluid elements restricted to cases with $S \approx 0$ or with $S \approx N$. The most probable values of the cosine of the angle between ω and β peak always at ± 1 , while the probability density of the cosine between ω and α or γ peaks at zero (and slightly more for γ). The alignment between ω and the intermediate eigenvector β increases with the stratification, and takes place in all fluid elements irrespectively of the region of the phase space they are visiting (although the alignment is better for fluid elements with $S \approx 0$ than for fluid elements at the brink of convection with $S \approx N$).

This could suggest that vortex stretching mechanisms in stably stratified turbulence are similar to those reported in homogeneous and isotropic turbulence. However, the alignment observed in

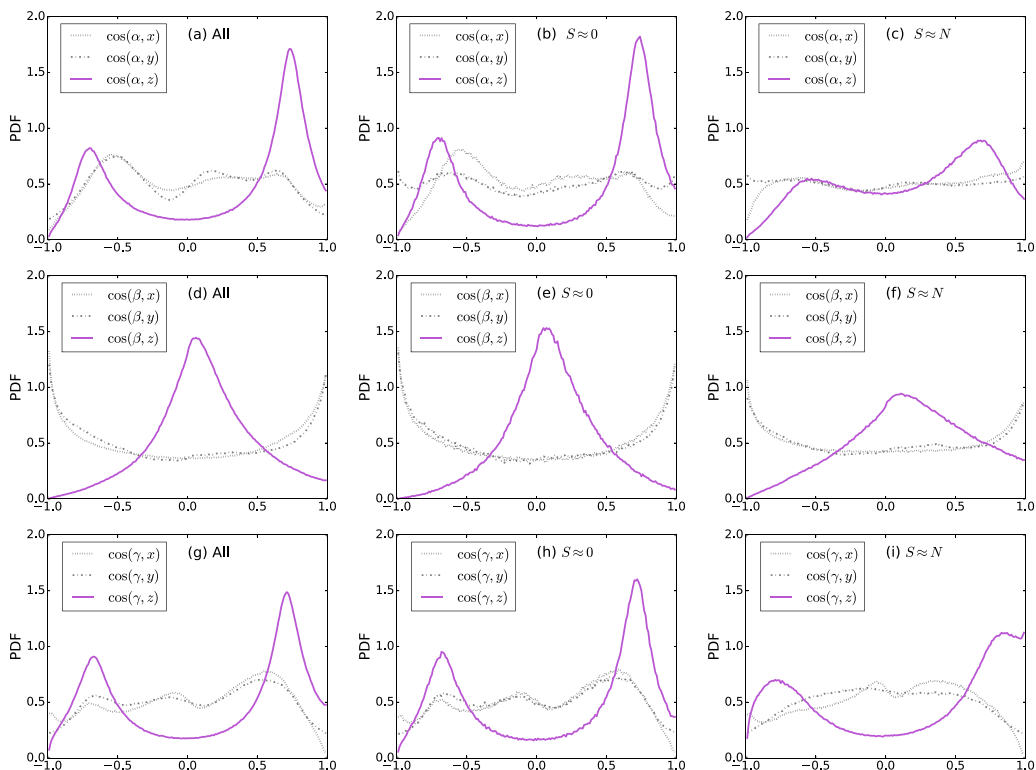


FIG. 11. PDFs of the cosine of the angles between the eigenvectors α , β , and γ of the strain rate tensor s_{ij} , and the Cartesian axes x , y , and z , for the simulation with $N = 8$. In the first row, panels (a)–(c) show the PDFs of the alignment between α and the Cartesian axes, for (a) all fluid elements, (b) fluid elements with $S \approx 0$, and (c) fluid elements with $S \approx N$. The second row, with panels (d)–(f), shows the same for the β eigenvector, while the third row, with panels (g)–(i), shows the same for γ .

Fig. 10 is, in this case, also related with the anisotropy of the flow. Indeed, the intermediate eigenvector β of the strain-rate tensor is preferentially perpendicular to gravity (which points in the z direction), and as a result also preferentially in the x - y plane (while the other two eigenvectors, α and γ , show a larger projection in z). This is shown in Fig. 11, which considers the statistics of the alignment between the eigenvectors of the strain-rate tensor and the x , y , and z axes for the simulation with $N = 8$. Note the differences between probability densities peaking near ± 1 (indicating the corresponding eigenvalue is mostly aligned with the axis considered), probability densities peaking near 0 (indicating the eigenvalue is mostly perpendicular to the axis considered), and flat probability densities denoting the absence of a clear correlation. The alignment of β with x or y happens on the average for the entire flow, and also in fluid elements in the Σ_1 (“wavy”) manifold, but less so in fluid elements in the Σ_0 (“convective”) manifold (see Fig. 11). This can be expected: Fluid elements in the “wavy” state have the eigenvectors with the largest and smallest strains pointing in the vertical direction (and thus, resulting in anisotropic structures), while interestingly, fluid elements at the brink of local convection display less alignment of α , β , and γ with the Cartesian axes (and as a result, of ω with these axes). While this speaks of a state in which the three Cartesian directions are more similar, note this does not result in a perfect isotropization (as peaks in the probability densities in Fig. 11 for fluid elements with $S \approx N$ are smaller than for all fluid elements or for the fluid elements with $S \approx 0$, but still visible). In spite of this, we can associate the second invariant manifold Σ_0 with flow regions that are more efficient at mixing.

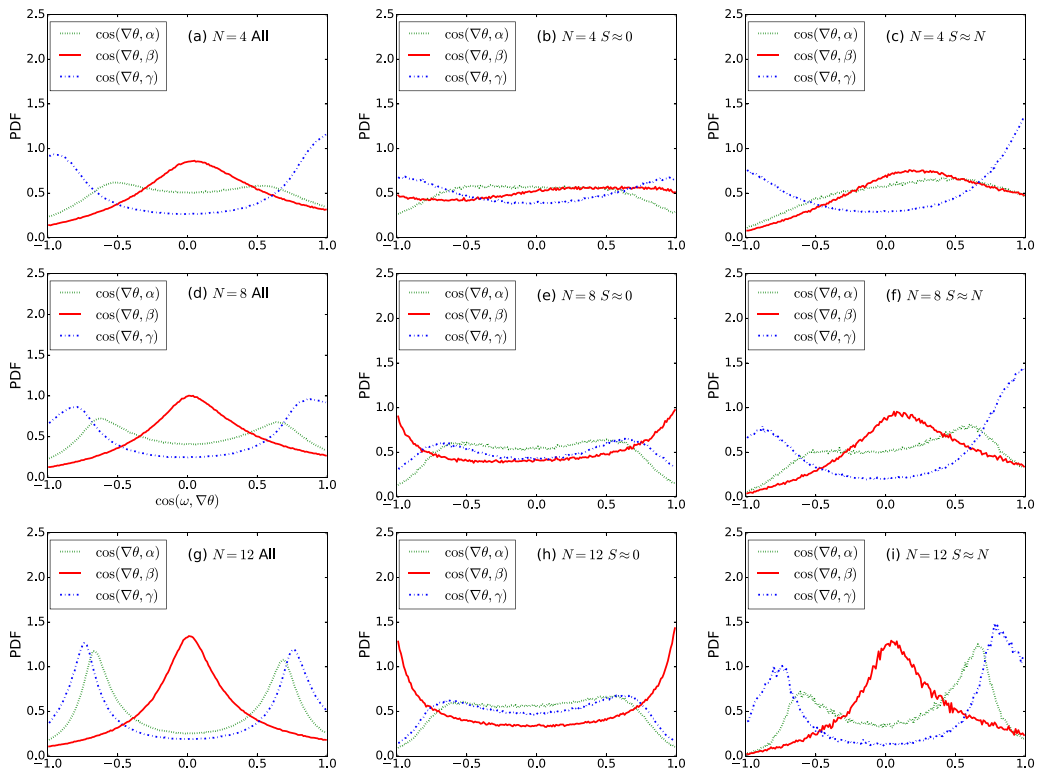


FIG. 12. PDFs of the cosine of the angles between the density gradient $\nabla\theta$ and the eigenvectors α , β , and γ of the strain rate tensor s_{ij} . In the first row, panels (a)–(c) show the PDFs for the simulation with $N = 4$, for (a) all fluid elements, (b) fluid elements with $S \approx 0$, and (c) fluid elements with $S \approx N$. The second row, with panels (d)–(f), shows the same PDFs for $N = 8$, while the third row, with panels (g)–(i), shows the same for $N = 12$.

Besides ω , in stably stratified turbulence we can also study the alignment of the vector defined by the buoyancy gradient $\nabla\theta$, with α , β , and γ . The vector $\nabla\theta$ provides us with information on how buoyancy changes in the vicinity of the fluid elements. In homogeneous and isotropic turbulence, when θ is a passive scalar, $\nabla\theta$ aligns preferentially with γ (the compressive strain direction) [62], which can be expected as compression increases the gradients of a scalar that is advected by the flow. Figure 12 shows the probability density functions of the cosine of the angle between $\nabla\theta$ and the eigenvectors of the strain-rate tensor in our simulations. On the average, for all fluid elements, $\nabla\theta$ is perpendicular to β and becomes more so as stratification increases. When all fluid elements are considered, $\nabla\theta$ also seems to align almost equally with either γ or α for strong stratification, which a small preference for aligning with γ (albeit this preference decreases with N). This can be related to the flow anisotropy, with gradients in the density fluctuations being mostly vertical and associated to the formation of strata or of pancakelike structures. But interestingly, we see again a strong difference in the alignment when fluid elements in the two invariant manifolds are considered separately. Now, fluid elements in the global invariant manifold Σ_0 ($S \approx N$) display a similar behavior as the average over all fluid elements (but with a stronger alignment with γ , as is observed in the case of passive scalars in homogeneous and isotropic turbulence [62]), while fluid elements in Σ_1 ($S \approx 0$) display the opposite trend and present a weak alignment of $\nabla\theta$ with β for sufficiently large N (and thus $\nabla\theta$ lies partially in the x - y plane). The latter behavior is to be expected for propagating internal gravity waves.

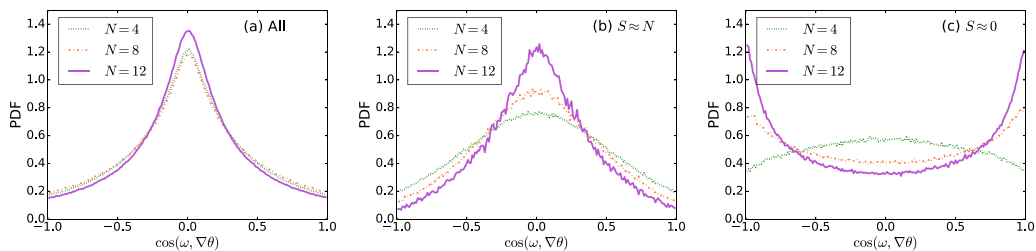


FIG. 13. Probability density functions of the cosine of the angle between the density gradient $\nabla\theta$ and the vorticity ω for all simulations in Table I, for (a) all fluid elements, (b) fluid elements with $S \approx 0$, and (c) fluid elements with $S \approx N$.

From these results, it can be expected that $\nabla\theta$ and ω should be perpendicular on the average, and display different behaviors in the two slow manifolds of the system. This is indeed seen in Fig. 13, which shows the probability density functions of the cosine of the angle between these two vectors in all numerical simulations. The probability densities peak at 0 for all fluid elements and when restricted to fluid elements in Σ_0 , while for fluid elements in Σ_1 (i.e., for wavelike behavior) these two vectors go from weakly perpendicular to strongly parallel as N is increased.

Besides giving information on the local geometry of the flow, and confirming that fluid elements are in different states when exploring the two invariant manifolds Σ_0 and Σ_1 , the results in this section also confirm a requirement for the validity of the reduced model in Eq. (23). When deriving this model, we reduced the information in the velocity gradient tensor A_{ij} and in the buoyancy gradient θ_i to seven scalars by using the fact that the flow has a preferred direction (given by the direction of stratification, or of gravity). Thus, scalar quantities defined in Eq. (16) treat differently A_{zz} , A_{iz} , A_{zi} , and θ_z , but not other components of these tensors and vectors involving the x or y Cartesian directions (in other words, we reduce the information in the tensors and vectors by using the axisymmetry of the equations). Probability density functions presented in this section confirm that there is a preference of the eigenvectors of the strain-rate tensor, and of other vectors, to align parallel or perpendicular to z , but with no clear preferences in the x or y direction.

VII. POTENTIAL VORTICITY

The relations reported above for field gradients in each of the invariant manifolds of the system also have implications for the evolution of the potential vorticity. In a stably stratified flow under the Boussinesq approximation, the potential vorticity is

$$\text{PV} = \omega \cdot \nabla\theta - N\omega_z = (S - N)(A_{yx} - A_{xy}) + \theta_x(A_{zy} - A_{yz}) + \theta_y(A_{xz} - A_{zx}), \quad (36)$$

which is a conserved quantity following fluid trajectories in the ideal (and unforced) case. The potential vorticity is an important quantity in geophysical flows as PV conservation, unlike circulation conservation or Kelvin's theorem, holds even for baroclinic flows. This makes the quantity of relevance for the atmosphere and the oceans. Indeed, PV is a scalar quantity that is advected by the flow and can be used as a means to track fluid elements, as well as to reconstruct the flow properties in the vicinity of the fluid elements [63,64].

From the previous section it is clear that $\omega \cdot \nabla\theta \approx 0$ in most of the phase space. The only exception being the Σ_1 stable manifold, where all gradients are small, and so $\text{PV} \approx 0$. We can further decompose the potential vorticity as

$$\text{PV} = \text{PV}_z + \text{PV}_{xy}, \quad (37)$$

where $\text{PV}_z = (S - N)(A_{yx} - A_{xy})$ and $\text{PV}_{xy} = \theta_x(A_{zy} - A_{yz}) + \theta_y(A_{xz} - A_{zx})$. Note that $\text{PV}_z = 0$ in Σ_0 . But if PV is conserved, this implies that as fluid elements explore phase space, then PV_{xy} must be anticorrelated with PV_z and must compensate for its changes. Moreover, even when PV is not

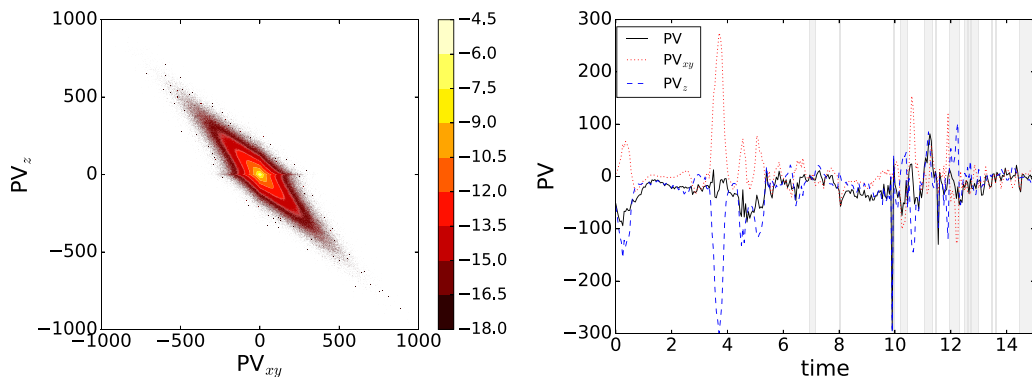


FIG. 14. Left: Joint probability density function of PV_{xy} and PV_z for all fluid elements in the simulation with $N = 4$. Right: Values of PV , PV_{xy} , and PV_z following a single particle trajectory in the simulation with $N = 4$. The value of PV fluctuates around zero, with sudden bursts of PV_{xy} and PV_z canceling each other. The grey areas indicate changes in sign of PV_{xy} (and thus also of PV_z) as a result of S becoming larger than N .

perfectly conserved (e.g., in the presence of dissipation), we can expect variations in PV to be slow compared with the fast evolution when fluid elements escape from one of the invariant manifolds to the other.

Indeed, Fig. 14 confirms this anticorrelation from data obtained from the direct numerical simulations with $N = 4$. On the average, $PV_z \approx -PV_{xy}$ for most fluid elements, and the most probable values in the joint probability density function of PV_z and PV_{xy} correspond to relatively small values of these quantities. Figure 14 also shows the time evolution of PV for a single fluid element in the same simulation, as a function of time, as well as the two components PV_z and PV_{xy} . The potential vorticity fluctuates around zero. However, sudden bursts of S (as those seen in Fig. 8) affect the evolution of PV_z , and as a result of PV_{xy} . Note how each sudden burst of PV_z has an associated burst of opposite sign of PV_{xy} , so that PV displays less fluctuations than the two components separately. In Fig. 14 we also shade some time intervals in which the change of sign of PV_z (and, as a consequence, also in PV_{xy}) is not due to S displaying a burst, but becoming instead larger than N , which can occur when fluid elements are in the vicinity of or escape from the “convective” manifold Σ_0 . The dynamic of these quantities is reminiscent of that observed in Fig. 8, with fluid elements displaying a slow evolution, with fast bursts that change the state from one regime to another.

VIII. CONCLUSIONS

Fluid elements in stably stratified turbulence explore a complicated phase space by moving between two places (associated with slow invariant manifolds). And these two places put fluid elements in two very different states. In the first manifold, fluid elements are in a quiet “wavy” state. When energy becomes sufficiently large, fluid elements escape from this manifold and evolve rapidly toward another manifold in which evolution is also slow. This second manifold is at the brink of the local convective instability, and thus can be expected to correspond to a disordered state characterized by efficient mixing and dissipation. Once the strength of gradients decreases again, fluid elements return rapidly to the first manifold. But as stratification is increased, the stability of the first manifold increases, and the journeys to the second manifold become less and less frequent.

The reduced system presented here, as well as the results from direct numerical simulations, indicate that the Boussinesq equations have only these two invariant manifolds, and as a result evolution outside these manifolds is fast. Such a picture, in which fluid elements explore slowly two solutions, and travel fast through the rest of phase space, is in good agreement with recent

developments in wave turbulence [40,41], and provide, at least for the case of stably stratified turbulence and in the full Boussinesq system, a much needed route for dissipation. While wavelike motions can bring energy to smaller scales, eventually the amplitude of the nonlinearity becomes such that the fluid elements must search for other surfaces of solutions in phase space. These solutions, which do not correspond to waves, dissipate energy efficiently, and fluid elements can then return to their previous state.

The existence of the second invariant manifold, which is at the brink of a convective instability, explains recent observations that a significant fraction of fluid elements in stratified turbulence is always at the threshold of a linear instability [5] or in a critical state [1,6], that only an intermittent fraction of fluid elements in the ocean are responsible for dissipation [3], and that extreme vertical drafts develop sporadically in these flows resulting in non-Gaussian statistics [4,11].

Besides, the invariant manifolds of the reduced system for the Lagrangian evolution of velocity and density gradients indicate that (1) Certain balance relations must hold as fluid elements are advected in the flow. These balance relations impose conditions, e.g., in the turbulent production of gradients of density fluctuations, with implications for subgrid models of turbulence. (2) The change of the invariant manifolds with respect to the homogeneous and isotropic case (and in particular, the destruction of the Vieillefosse tail), modifies the geometry of vortex stretching, thus providing a different explanation for the change in vortical structures and the development of pancakelike structures as stratification is increased. Moreover, these changes are different depending on what region of phase space the fluid elements are exploring. And (3), correlations exist in the evolution of different terms in the potential vorticity, as fluid elements travel from one manifold to the other.

The model also has clear limitations. The first is that it neglects the effect of forcing and dissipation. This can be also seen as an advantage, as an external forcing could obscure the evolution or drive the system into solutions that are not preferred by the partial differential equations. The second is that pressure gradient effects are partially neglected (as the deviatoric part of the pressure Hessian is dropped). This second limitation is shared with restricted Euler models of homogeneous and isotropic turbulence [43–45], although in the stably stratified case the role of the pressure Hessian is smaller as stratification is increased. In spite of these limitations, it is interesting that direct numerical simulations of the full Boussinesq equations including forcing and dissipation are in agreement with predictions from the model. This suggests that some of the manifolds and balance relations that follow from the model could be used for the development of subgrid models (as an example, to derive new estimations for turbulent production of vertical density fluctuations), as predictors of the occurrence of extreme events such as those observed in clean air turbulence or in extreme vertical updrafts and downdrafts, or to explain the origin of the anomalous dissipation reported in recent oceanic models.

ACKNOWLEDGMENT

The authors acknowledge support from PICT Grant No. 2015-3530.

-
- [1] W. D. Smyth and J. N. Moum, Marginal instability and deep cycle turbulence in the eastern equatorial pacific ocean, *Geophys. Res. Lett.* **40**, 6181 (2013).
 - [2] C. Rorai, P. D. Mininni, and A. Pouquet, Turbulence comes in bursts in stably stratified flows, *Phy. Rev. E* **89**, 043002 (2014).
 - [3] B. Pearson and B. Fox-Kemper, Log-Normal Turbulence Dissipation in Global Ocean Models, *Phys. Rev. Lett.* **120**, 094501 (2018).
 - [4] F. Feraco, R. Marino, A. Pumir, L. Primavera, P. D. Mininni, A. Pouquet, and D. Rosenberg, Vertical drafts and mixing in stratified turbulence: Sharp transition with froude number, *Europhys. Lett.* **123**, 44002 (2018).

-
- [5] A. Pouquet, D. Rosenberg, and R. Marino, Linking dissipation, anisotropy, and intermittency in rotating stratified turbulence at the threshold of linear shear instabilities, *Phys. Fluids* **31**, 105116 (2019).
- [6] W. D. Smyth, J. D. Nash, and J. N. Moum, Self-organized criticality in geophysical turbulence, *Sci. Rep.* **9**, 3747 (2019).
- [7] P. Bauer, A. Thorpe, and G. Brunet, The quiet revolution of numerical weather prediction, *Nature* **525**, 47 (2015).
- [8] E. Bodenschatz, S. P. Malinowski, R. A. Shaw, and F. Stratmann, Can we understand clouds without turbulence? *Science* **327**, 970 (2010).
- [9] M. L. Waite and P. Bartello, Stratified turbulence dominated by vortical motion, *J. Fluid Mech.* **517**, 281 (2004).
- [10] J. J. Riley and E. Lindborg, Stratified turbulence: A possible interpretation of some geophysical turbulence measurements, *J. Atmos. Sci.* **65**, 2416 (2008).
- [11] C. Rorai, P. D. Mininni, and A. Pouquet, Stably stratified turbulence in the presence of large-scale forcing, *Phys. Rev. E* **92**, 013003 (2015).
- [12] A. Pouquet, D. Rosenberg, R. Marino, and C. Herbert, Scaling laws for mixing and dissipation in unforced rotating stratified turbulence, *J. Fluid Mech.* **844**, 519 (2018).
- [13] S. M. de Bruyn Kops and J. J. Riley, The effects of stable stratification on the decay of initially isotropic homogeneous turbulence, *J. Fluid Mech.* **860**, 787 (2019).
- [14] F. S. Godeferd and C. Cambon, Detailed investigation of energy transfers in homogeneous stratified turbulence, *Phys. Fluids* **6**, 2084 (1994).
- [15] L. M. Smith and F. Waleffe, Generation of slow large scales in forced rotating stratified turbulence, *J. Fluid Mech.* **451**, 145 (2002).
- [16] R. Godoy-Diana, J.-M. Chomaz, and P. Billant, Vertical length scale selection for pancake vortices in strongly stratified viscous fluids, *J. Fluid Mech.* **504**, 229 (2004).
- [17] R. Marino, P. D. Mininni, D. L. Rosenberg, and A. Pouquet, Large-scale anisotropy in stably stratified rotating flows, *Phys. Rev. E* **90**, 023018 (2014).
- [18] G. N. Ivey, K. B. Winters, and J. R. Koseff, Density stratification, turbulence, but how much mixing? *Annu. Rev. Fluid Mech.* **40**, 169 (2008).
- [19] G. Falkovich, H. Xu, A. Pumir, E. Bodenschatz, L. Biferale, G. Boffetta, A. S. Lanotte, F. Toschi, and (International Collaboration for Turbulence Research), On Lagrangian single-particle statistics, *Phys. Fluids* **24**, 055102 (2012).
- [20] M. Chertkov, A. Pumir, and B. I. Shraiman, Lagrangian tetrad dynamics and the phenomenology of turbulence, *Phys. Fluids* **11**, 2394 (1999).
- [21] F. Toschi and E. Bodenschatz, Lagrangian properties of particles in turbulence, *Annu. Rev. Fluid Mech.* **41**, 375 (2009).
- [22] H. Xu, A. Pumir, and E. Bodenschatz, The pirouette effect in turbulent flows, *Nat. Phys.* **7**, 709 (2011).
- [23] Y. Kimura and J. R. Herring, Diffusion in stably stratified turbulence, *J. Fluid Mech.* **328**, 253 (1996).
- [24] M. van Aartrijk, H. J. H. Clercx, and K. B. Winters, Single-particle, particle-pair, and multiparticle dispersion of fluid particles in forced stably stratified turbulence, *Phys. Fluids* **20**, 025104 (2008).
- [25] N. E. Sujovolsky, P. D. Mininni, and M. P. Rast, Single-particle dispersion in stably stratified turbulence, *Phys. Rev. Fluids* **3**, 034603 (2018).
- [26] N. E. Sujovolsky and P. D. Mininni, Vertical dispersion of Lagrangian tracers in fully developed stably stratified turbulence, *Phys. Rev. Fluids* **4**, 014503 (2019).
- [27] D. Buaria, A. Pumir, F. Feraco, R. Marino, A. Pouquet, D. Rosenberg, and L. Primavera, Single-particle Lagrangian statistics from direct numerical simulations of rotating-stratified turbulence, *Phys. Rev. Fluids* **5**, 064801 (2020).
- [28] E. A. D'Asaro and R.-C. Lien, Lagrangian measurements of waves and turbulence in stratified flows, *J. Phys. Oceanogr.* **30**, 641 (2000).
- [29] R.-C. Lien and E. A. D'Asaro, Measurement of turbulent kinetic energy dissipation rate with a Lagrangian float, *J. Atmos. Ocean. Tech.* **23**, 964 (2006).
- [30] N. E. Sujovolsky, G. B. Mindlin, and P. D. Mininni, Invariant manifolds in stratified turbulence, *Phys. Rev. Fluids* **4**, 052402 (2019).

- [31] Y. Kaneda and T. Ishida, Suppression of vertical diffusion in strongly stratified turbulence, *J. Fluid Mech.* **402**, 311 (2000).
- [32] C. Cambon, F. S. Godeferd, F. C. G. A. Nicolleau, and J. C. Vassilicos, Turbulent diffusion in rapidly rotating flows with and without stable stratification, *J. Fluid Mech.* **499**, 231 (2004).
- [33] A. Salhi and C. Cambon, Anisotropic phase-mixing in homogeneous turbulence in a rapidly rotating or in a strongly stratified fluid: An analytical study, *Phys. Fluids* **19**, 055102 (2007).
- [34] P. Sagaut and C. Cambon, *Homogeneous Turbulence Dynamics* (Springer, Berlin, 2008).
- [35] P. A. Davidson, *Turbulence in Rotating, Stratified and Electrically Conducting Fluids* (Cambridge University Press, Cambridge, UK, 2013).
- [36] J. J. Riley, R. W. Metcalfe, and M. A. Weissman, Direct numerical simulations of homogeneous turbulence in density-stratified fluids, *Nonlinear Properties of Internal Waves: La Jolla Institute, 1981*, edited by B. J. West, AIP Conf. Proc. No. 76 (AIP, New York, 1981), p. 79.
- [37] M.-P. Lelong and J. J. Riley, Internal wave-vortical mode interactions in strongly stratified flows, *J. Fluid Mech.* **232**, 1 (1991).
- [38] C. Herbert, R. Marino, D. Rosenberg, and A. Pouquet, Waves and vortices in the inverse cascade regime of stratified turbulence with or without rotation, *J. Fluid Mech.* **806**, 165 (2016).
- [39] S. Nazarenko, *Wave Turbulence* (Springer Science & Business Media, New York, 2011).
- [40] A. C. Newell and B. Rumpf, Wave turbulence: A story far from over, in *Advances in Wave Turbulence* (World Scientific, Singapore, 2013).
- [41] S. Dyachenko and A. C. Newell, Whitecapping, *Studies Appl. Math.* **137**, 199 (2016).
- [42] P. Vieillefosse, Local interaction between vorticity and shear in a perfect incompressible fluid, *J. Physique* **43**, 837 (1982).
- [43] B. J. Cantwell, Exact solution of a restricted Euler equation for the velocity gradient tensor, *Phys. Fluids A* **4**, 782 (1992).
- [44] L. Chevillard and C. Meneveau, Lagrangian dynamics and statistical geometric structure of turbulence, *Phys. Rev. Lett.* **97**, 174501 (2006).
- [45] C. Meneveau, Lagrangian dynamics and models of the velocity gradient tensor in turbulent flows, *Annu. Rev. Fluid Mech.* **43**, 219 (2011).
- [46] M. Wilczek and C. Meneveau, Pressure hessian and viscous contributions to velocity gradient statistics based on gaussian random fields, *J. Fluid Mech.* **756**, 191 (2014).
- [47] P. L. Johnson and C. Meneveau, A closure for lagrangian velocity gradient evolution in turbulence using recent-deformation mapping of initially gaussian fields, *J. Fluid Mech.* **804**, 387 (2016).
- [48] R. M. Pereira, L. Moriconi, and L. Chevillard, A multifractal model for the velocity gradient dynamics in turbulent flows, *J. Fluid Mech.* **839**, 430 (2018).
- [49] D. Rosenberg, A. Pouquet, R. Marino, and P. D. Mininni, Evidence for Bolgiano-Obukhov scaling in rotating stratified turbulence using high-resolution direct numerical simulations, *Phys. Fluids* **27**, 055105 (2015).
- [50] P. Billant and J.-M. Chomaz, Theoretical analysis of the zigzag instability of a vertical columnar vortex pair in a strongly stratified fluid, *J. Fluid Mech.* **419**, 29 (2000).
- [51] A. Mashayek, H. Salehipour, D. Bouffard, C. P. Caulfield, R. Ferrari, M. Nikurashin, W. R. Peltier, and W. D. Smyth, Efficiency of turbulent mixing in the abyssal ocean circulation, *Geophys. Res. Lett.* **44**, 6296 (2017).
- [52] P. D. Mininni, D. Rosenberg, R. Reddy, and A. Pouquet, A hybrid MPI–OpenMP scheme for scalable parallel pseudospectral computations for fluid turbulence, *Parallel Comput.* **37**, 316 (2011).
- [53] J. J. Riley and S. M. deBruynKops, Dynamics of turbulence strongly influenced by buoyancy, *Phys. Fluids* **15**, 2047 (2003).
- [54] N. E. Sujovolsky, P. D. Mininni, and A. Pouquet, Generation of turbulence through frontogenesis in sheared stratified flows, *Phys. Fluids* **30**, 086601 (2018).
- [55] P. K. Yeung and S. B. Pope, An algorithm for tracking fluid particles in numerical simulations of homogeneous turbulence, *J. Comput. Phys.* **79**, 373 (1988).

- [56] G. Gulitski, M. Kholmyansky, W. Kinzelbach, B. Lüthi, A. Tsinober, and S. Yorish, Velocity and temperature derivatives in high-Reynolds-number turbulent flows in the atmospheric surface layer. Part 3. Temperature and joint statistics of temperature and velocity derivatives, *J. Fluid Mech.* **589**, 103 (2007).
- [57] S. Wiggins, *Introduction to Applied Nonlinear Dynamical Systems and Chaos* (Springer Science & Business Media, New York, 2003).
- [58] M. S. Chong, A. E. Perry, and B. J. Cantwell, A general classification of three-dimensional flow fields, *Phys. Fluids A* **2**, 765 (1990).
- [59] V. Dallas and A. Alexakis, Structures and dynamics of small scales in decaying magnetohydrodynamic turbulence, *Phys. Fluids* **25**, 105106 (2013).
- [60] E. Lindborg and G. Brethouwer, Vertical dispersion by stratified turbulence, *J. Fluid Mech.* **614**, 303 (2008).
- [61] R. Marino, P. D. Mininni, D. Rosenberg, and A. Pouquet, Emergence of helicity in rotating stratified turbulence, *Phys. Rev. E* **87**, 033016 (2013).
- [62] W. T. Ashurst, A. R. Kerstein, R. M. Kerr, and C. H. Gibson, Alignment of vorticity and scalar gradient with strain rate in simulated Navier–Stokes turbulence, *Phys. Fluids* **30**, 2343 (1987).
- [63] G. K. Vallis, *Atmospheric and Oceanic Fluid Dynamics* (Cambridge University Press, Cambridge, UK, 2017).
- [64] M. L. Waite, Potential enstrophy in stratified turbulence, *J. Fluid Mech.* **722**, R4 (2013).